ADVANCED ENERGY MATERIALS

Supporting Information

for *Adv. Energy Mater.,* DOI: 10.1002/aenm.201701616

High-Performance Solar Steam Device with Layered Channels: Artificial Tree with a Reversed Design

*He Liu, Chaoji Chen, Guang Chen, Yudi Kuang, Xinpeng Zhao, Jianwei Song, Chao Jia, Xu Xu, Emily Hitz, Hua Xie, Sha Wang, Feng Jiang, Tian Li, Yiju Li, Amy Gong, Ronggui Yang, Siddhartha Das, and Liangbing Hu**

Supplementary Information for

High-Performance Solar Steam Device with Layered Channels: Artificial Tree with a Reversed Design

He Liu,[1a] Chaoji Chen,[1a] Guang Chen,[2] Yudi Kuang,[1] Xinpeng Zhao,[3] Jianwei Song,[1] Chao Jia,[1] Xu Xu,[1] Emily Hitz,[1] Hua Xie,[1] Sha Wang,[1] Feng Jiang,[1] Tian Li,[1] Yiju Li,[1] Amy Gong,[1] Ronggui Yang,[3] Siddhartha Das,[2] Liangbing Hu[1*]

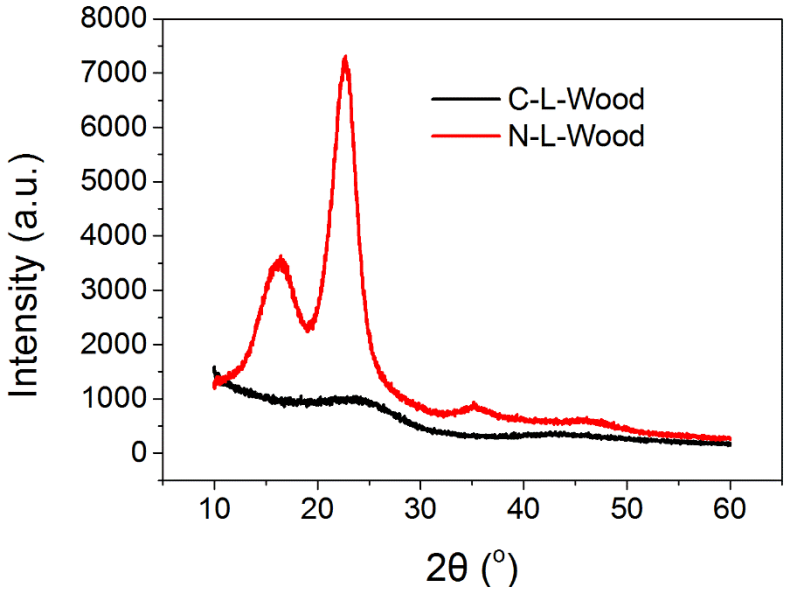

Figure S1. XRD patterns of carbonized wood layer and natural wood layer. The crystallinity of carbonized wood increases because the graphite structure arranges more closely after carbonization.

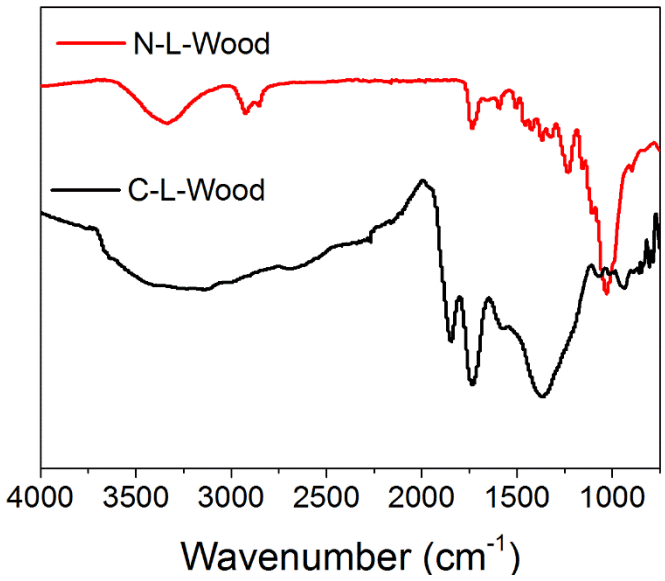

Figure S2. FT-IR spectra of the carbonized wood layer and natural wood layer. The wide peak range from 3000-3500 cm^{-1} indicates that the free hydroxyl group of wood reduces significantly. The peak at 1750 cm^{-1} suggests that the wood has been oxidized after carbonization.

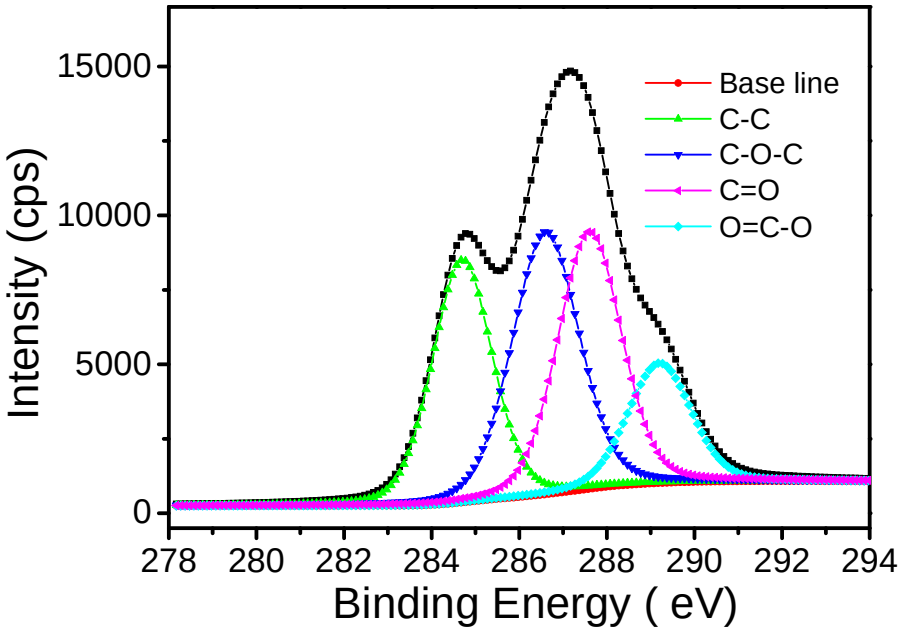

Figure S3. High-resolution XPS spectrum of C 1s in natural wood layer. XPS is employed to investigate the surface chemical composition of natural wood and carbonized wood. The C 1s spectrum can be deconvoluted into four peaks corresponding to C-C with a binding energy of 284.5 eV, O-C-O with a binding energy of 286.6 eV, C=O with a binding energy of 287.6 eV and O=C-O with a binding energy of 289.2 eV.

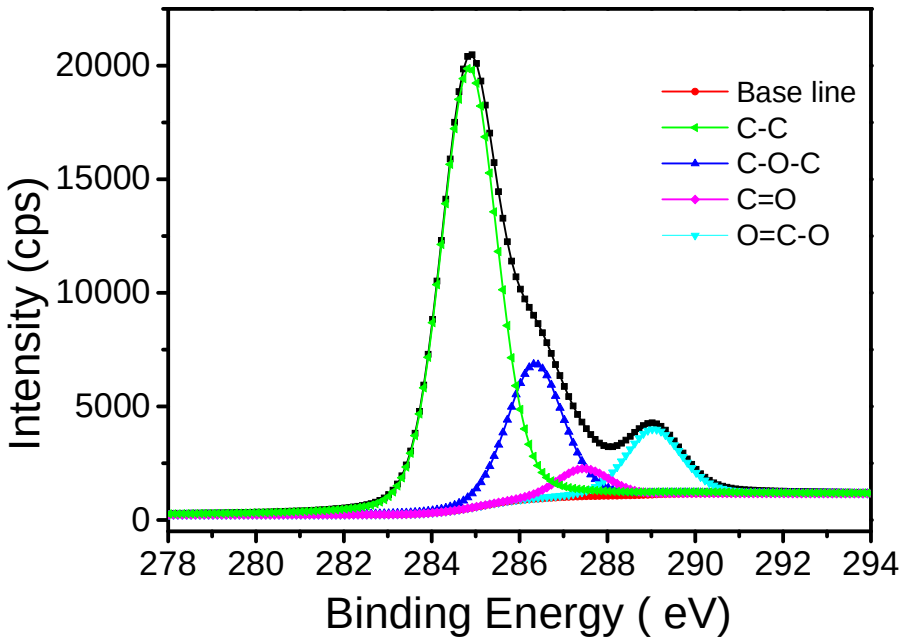

Figure S4. High-resolution XPS spectrum of C 1s in carbonized wood layer. The significant intensity increase of C-C groups at the surface confirm the successful carbonization of wood.

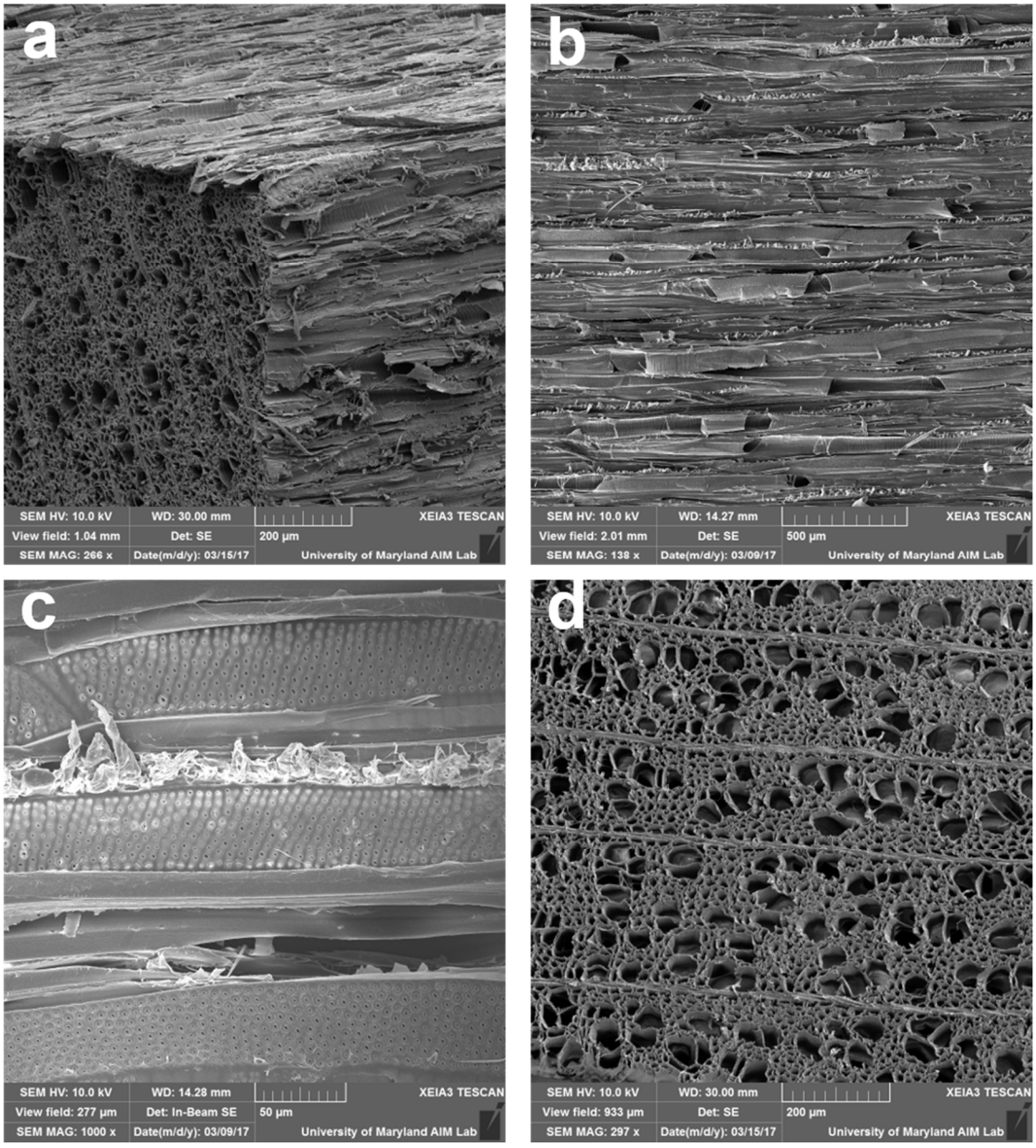

Figure S5. SEM images of natural wood. (a,b) Cross-sectional view image shows multiple aligned channels along the tree-growth direction. (c) Magnified SEM image shows that numerous nanopores exist on the channel walls. (d) Top-view SEM image shows the hierarchical channels with a bimodal pore size distribution of 20-50 µm and 5-10 µm, respectively.

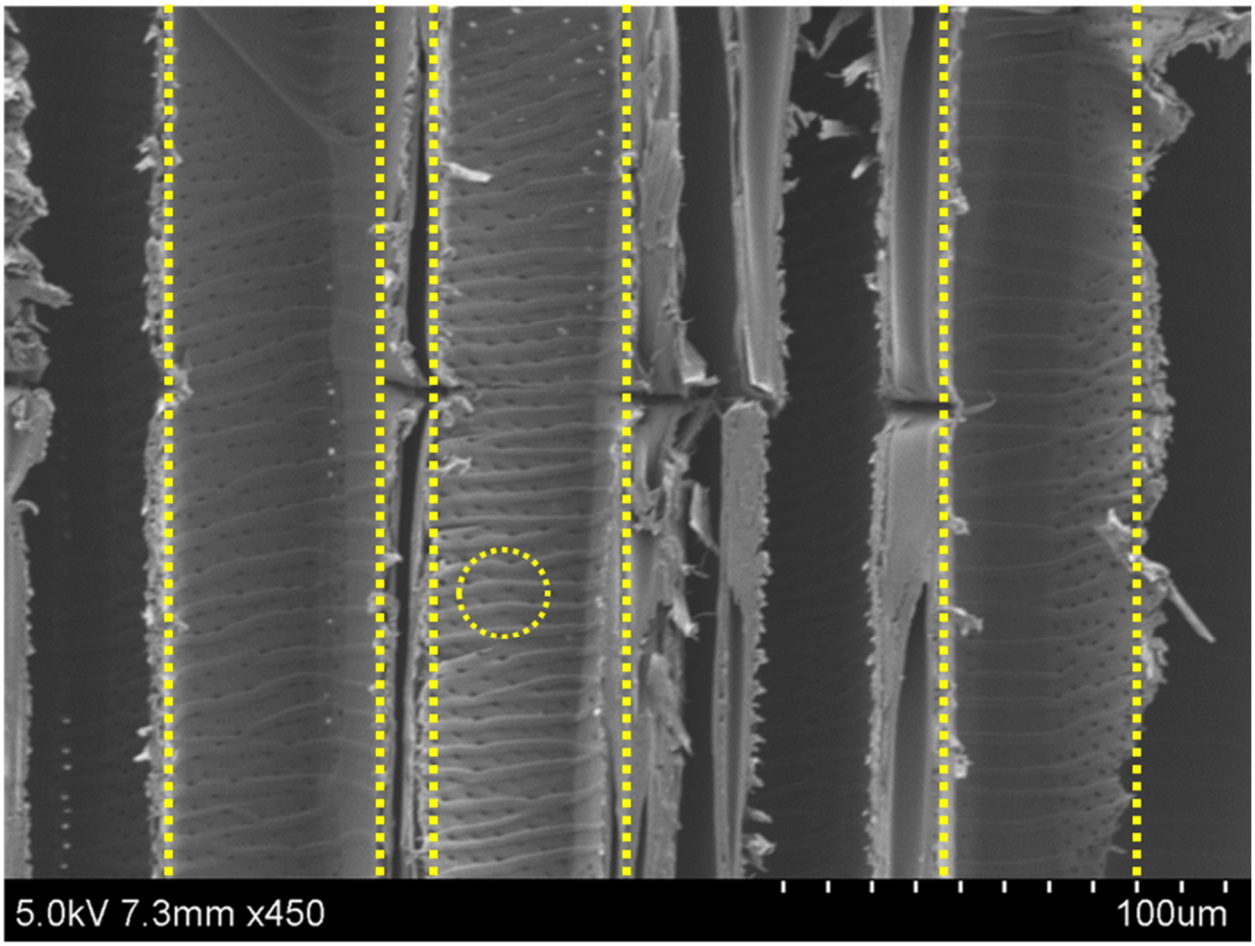

Figure S6. SEM image of the C-L-Wood shows the aligned vessels (channels) along the tree growth direction with numerous nanopores on the channel walls. The big channels along with the small pores lead to a 3D interconnected porous structure in the wood structure, enabling both longitudinal (tree-growth direction) and horizontal (vertical-to-tree-growth direction) water transportation.

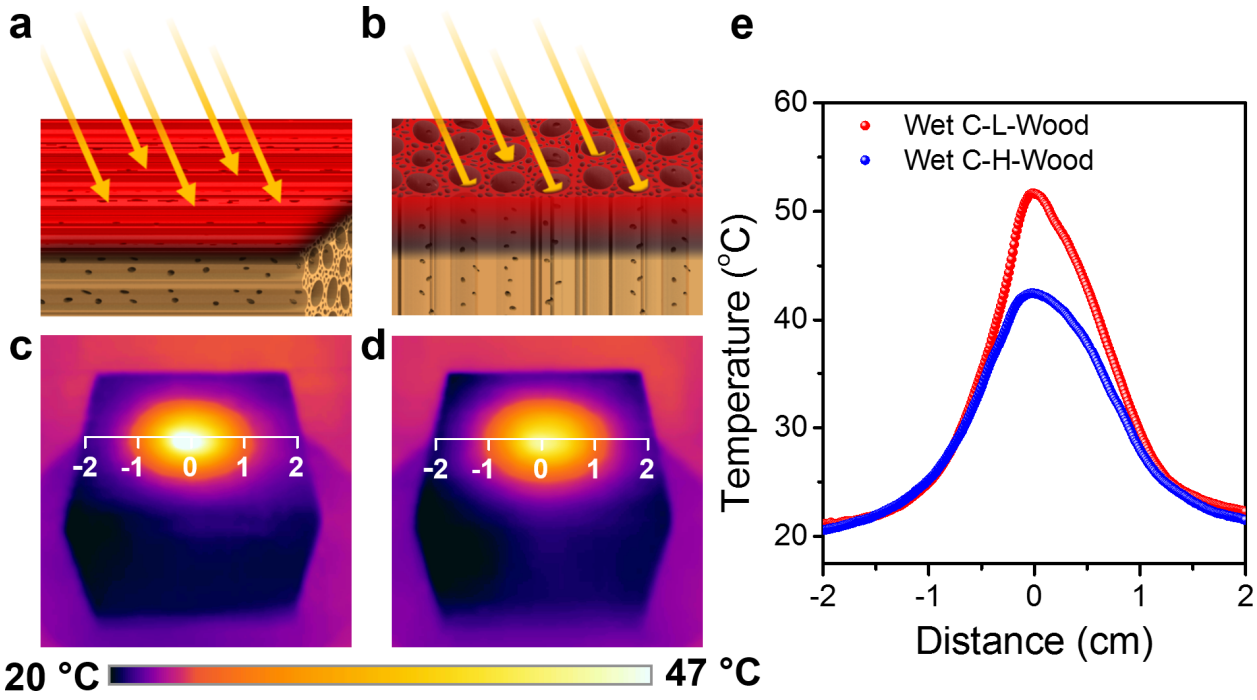

Figure S7. (a) Schematic illustration of heat localization on the C-L-Wood surface. (b) Schematic illustration of heat transfer along the C-H-Wood channels. (c) IR image of the top surface of wet C-L-Wood under three-sun irradiation. (d) IR image of the top surface of wet C-H-Wood under three-sun irradiation. (e) The temperature profile on the top surface for both wet C-L-Wood and wet C-H-Wood as a function of distance from the illumination center. It is also found that the maximum temperature on the top surface for the wet C-L-Wood is as high as 52°C, which is also 10°C higher than that of the wet C-H-Wood after 600 s of three-sun irradiation. It indicates that the localization of the generated heat upon solar irradiation is due to the excellent thermal barrier created by the layered channel structure of the C-L-Wood. Thus, more photothermally-converted heat in the C-H-Wood can be conducted along the channel walls with aligned cellulose fibrils.

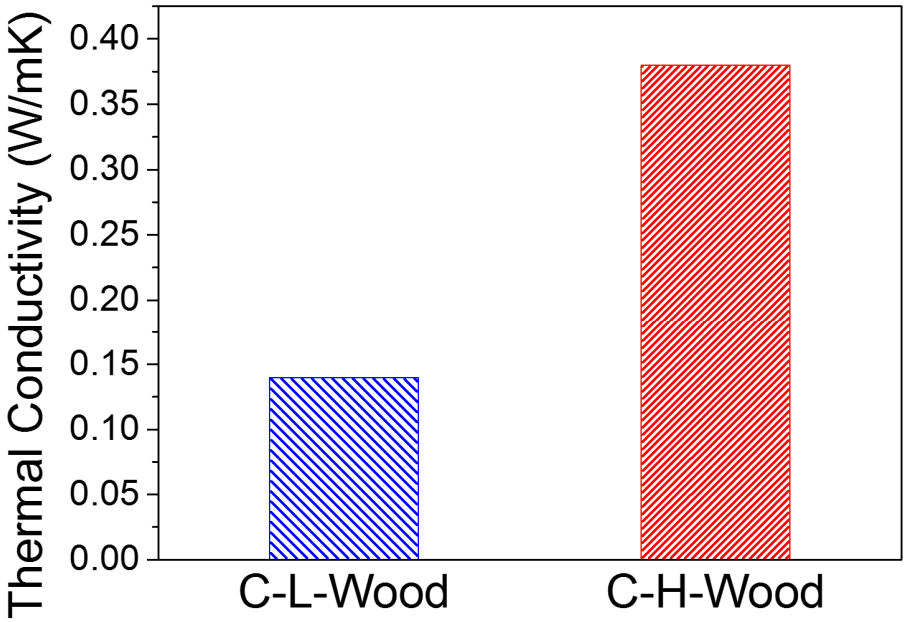

Figure S8. Thermal conductivities of the C-L-Wood and C-H-Wood under 5-sun irradiation after 4 h of operation of solar steam generation. The thermal conductivities of the C-L-Wood and C-H-Wood under dynamic operating conditions are 0.14 W mK^{-1} and 0.38 W mK^{-1}, respectively. The test results indicated that the C-L-Wood exhibits a better thermal insulating property than that of C-H-Wood even under dynamic operating condition.

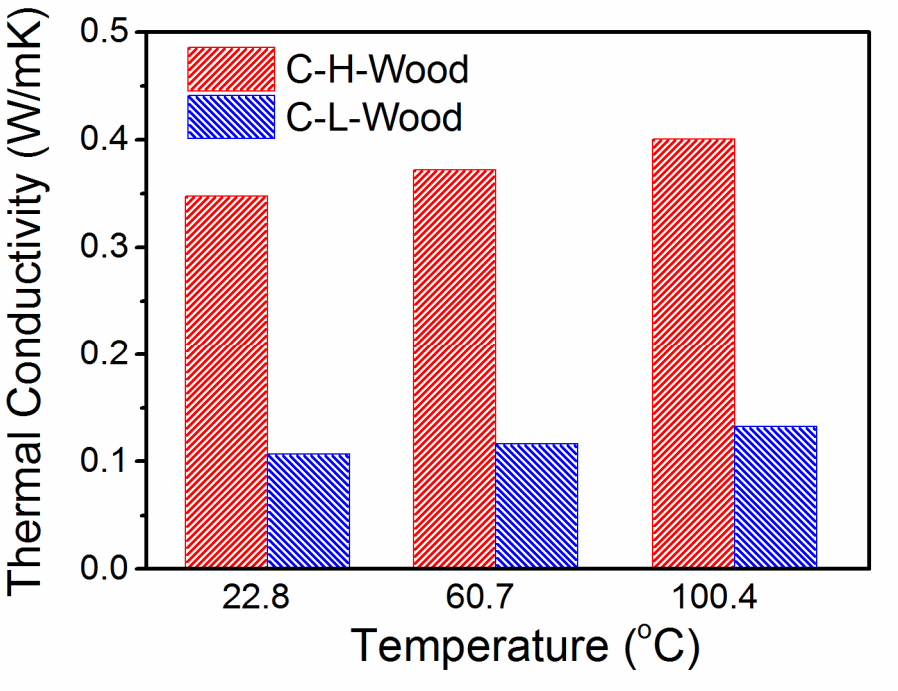

Figure S9. Thermal conductivities versus temperature of the C-L-Wood and C-H-Wood. The thermal conductivities of both samples slightly increase as the temperature gets higher. Compared to the C-H-Wood (horizontal), the C-L-Wood (longitudinal) has lower (~1/3) thermal conductivities at all tested temperatures, suggesting a better thermal insulating property of the C-L-Wood.

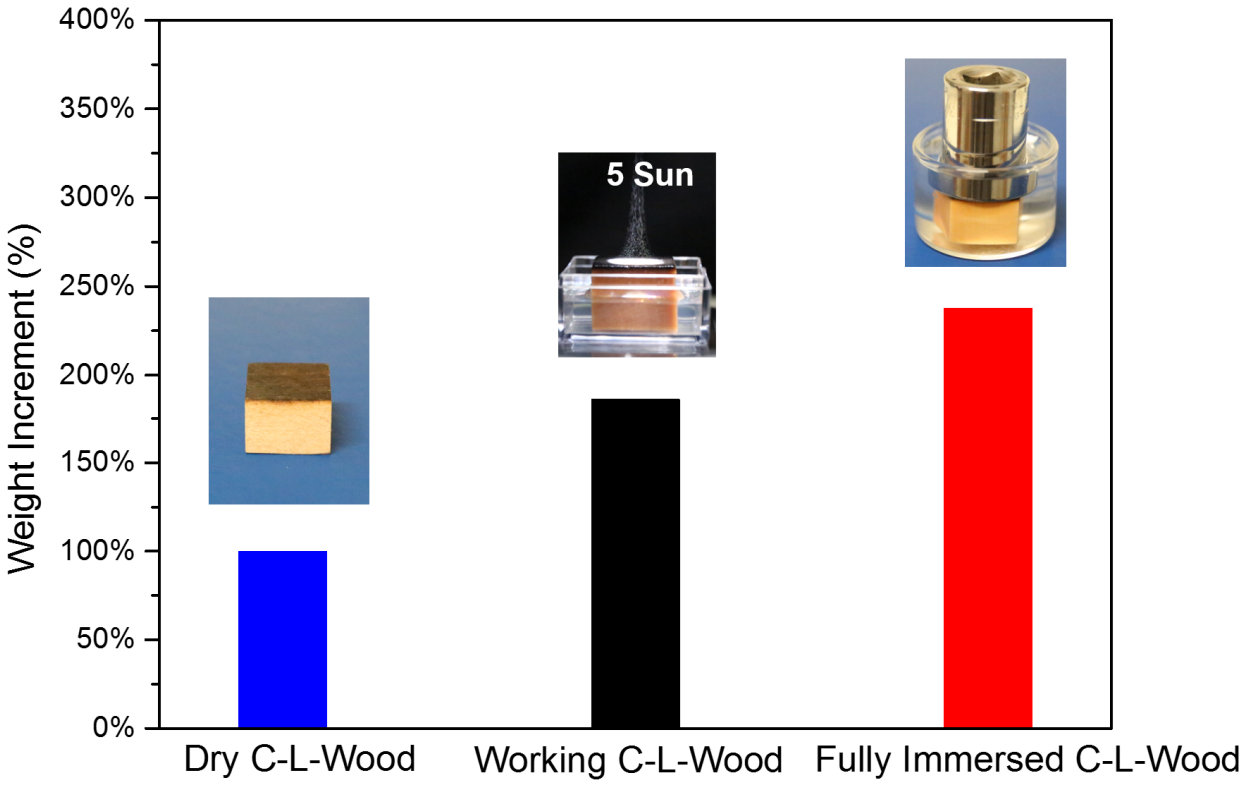

Figure S10. Relative weight of the C-L-Wood block under 5 sun irradiation for 4 h (Working C-L-Wood) and totally immersed in water for 4 h (Fully immersed C-L-Wood) compared to their dry counterparts.

Numerical Simulation details and further discussions

3-D Numerical simulations for the flow through the wood structure (see Fig. 3g) are carried out by solving the coupled Navier-Stokes and continuity equations:

$$\nabla \cdot \mathbf{u} = 0$$

$$\rho(\mathbf{u}\cdot\nabla)\mathbf{u} = -\nabla\cdot(p\mathbf{I}) + \nabla\cdot(\mu\nabla\mathbf{u})$$

Here $\mathbf{u}$ is the flow velocity vector, p is the pressure, ρ and μ are the density and dynamic viscosity of water. The solutions are carried out in presence of the boundary conditions explicated in Fig. 3g.

Figures S11b and c demonstrate our experimental results on how the variation in the height h (see Fig. S11a) affects the evaporation rate (E.R.). When h is small (see Fig. S11b), E.R. is smaller than the capillary filling rate at the top of the wood surface. This stems from the fact that the top of the wood surface, being at a smaller height from the water free surface, experiences a larger capillary-driven water velocity and hence a larger capillary filling rate (F.R.). As a consequence, E.R. progressively increases with time, albeit the rate of increase is slow at smaller times. On the contrary, when h is larger (see Fig. S11c) the F.R. at the top of the wood surface is smaller. As a consequence, the E.R. first increases with time, then decreases, and finally saturates to a constant equilibrium value. The equilibrium suggests, E.R. = F.R. Consequently, this equilibrium E.R. (~14 kg m^{-2} h^{-1}) is the equilibrium F.R., which in turn corresponds to a filling velocity of 3.9 μm/s (obtained by diving this F.R. by water density of 1000 kg/m^3).

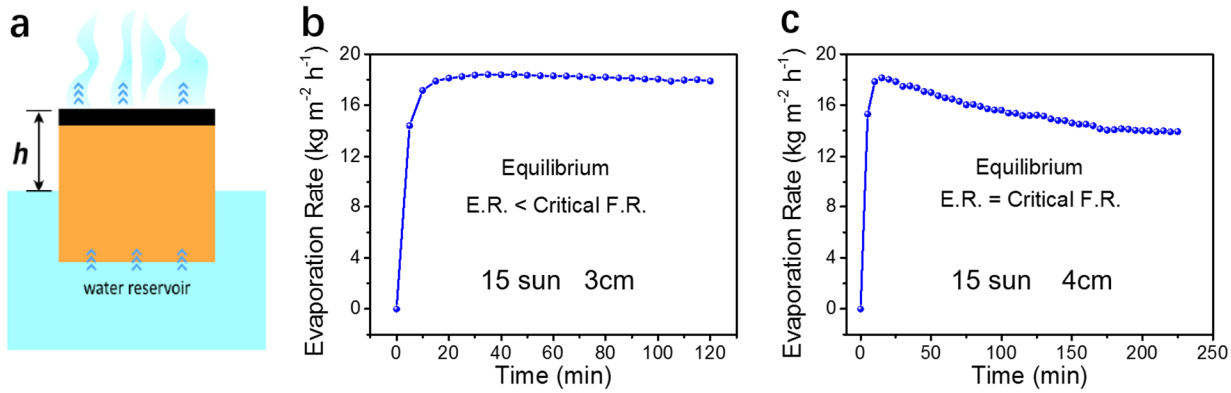

Figure S11. (a) Cartoon showing the wood-block-driven evaporation. (b) The time-dependent evaporation rate for h = 3 cm and irradiation of 15 Sun. (c) The time-dependent evaporation rate for h = 4 cm and irradiation of 15 Sun.

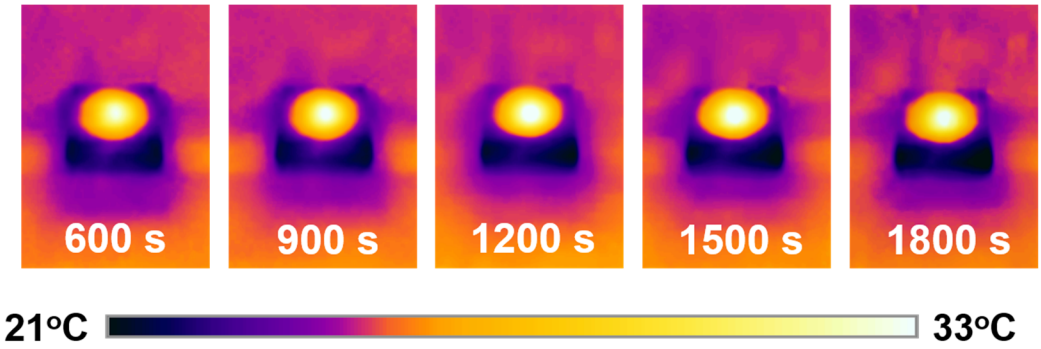

Figure S12. IR images showing the temperature of the water and the C-L-Wood floated at the air/water interface under one-sun solar illumination at the time range of 600-1800 s. The temperature of the top surface of the C-L-Wood remains approximately constant around 30.5°C from 600 s to 1800 s.

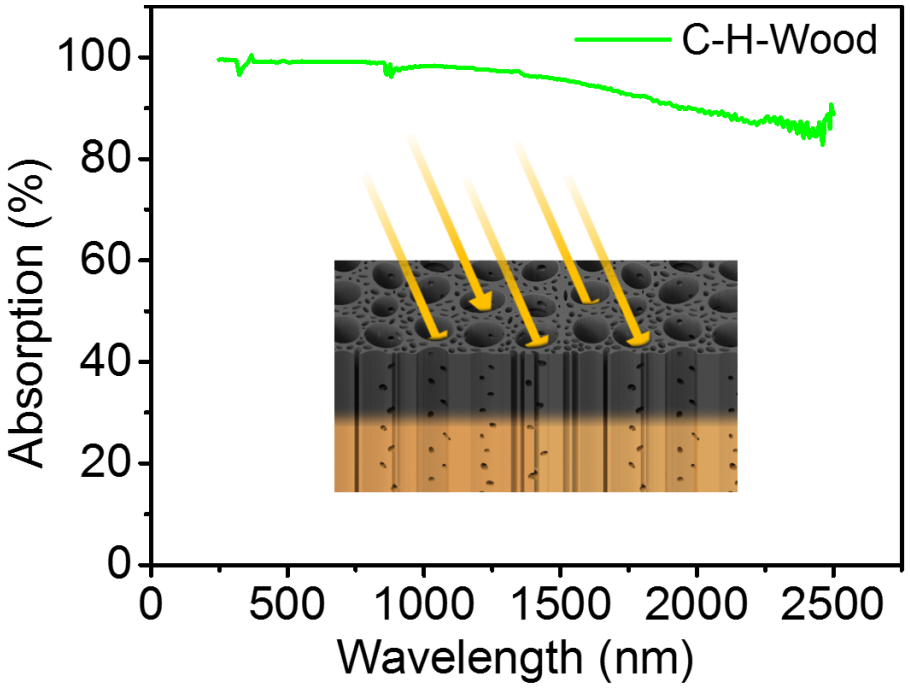

Figure S13. Experimentally measured light absorption spectra for C-H-Wood. In a wavelength range of 300-1400 nm where the solar radiation is mainly distributed, the absorption of C-H-Wood reaches higher value of more than 98 %.

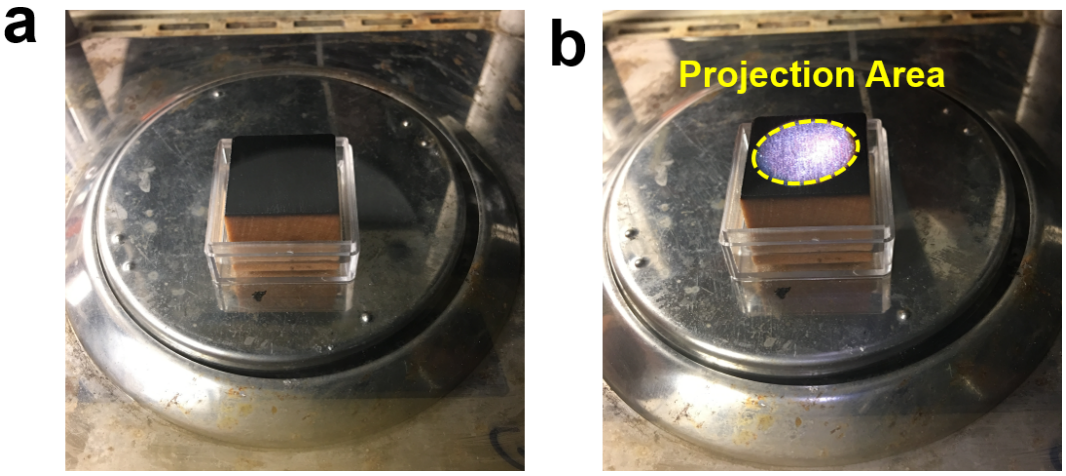

Figure S14. (a) Digital image of natural water vaporization of C-L-Wood solar steam generation device on an electronic balance without sunlight. (b) Digital image of water vaporization of C-L-Wood solar steam generation device on an electronic balance under one-Sun irradiation.

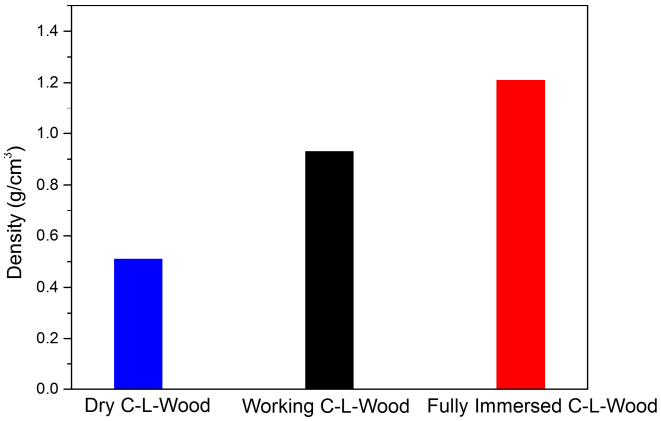

Figure S15. Densities of the C-L-Wood under dry, working, and totally immersed conditions.

Table S1. Comparisons of efficiency, price, and scalability of various steam-generation devices.

Material	efficiency	Price	Scalability	Ref.
Surface carbonized longitudinal wood	**74% under 1 sun, 89% under 10 sun**	**low**	**large**	**This work**
Nanoporous anodic aluminium oxide membrane (AAM) close packed aluminium NPs.	57% under 1 sun, 88.4% under 4 sun, 91% under 6 sun	medium	small	1
Airlaid-paper-based AuNP film (PGF)	~77.8% under 4.5 sun	high	medium	2
A bilayered hybrid biofoam composed of bacterial nanocellulose (BNC) and RGO	83% under 10 sun	high	medium	3
The carbon-black-based super-hydrophobic gauze	—	high	medium	4
Nanosized titanium sesquioxide (Ti_2O_3) /cellulose membrane (CM)	<65% under 1 sun, <75% under 5 sun	high	medium	5
Graphene oxide (GO)/ biocompatible sodium alginate(SA)/ multi-walled carbon nanotubes (MWCNTs) aerogels	85% under 1 sun	high	medium	6
GO/polystyrene foam	80% under 1 sun	high	medium	7
3D porous graphene sheets particularly with nitrogen doping	80% under 1 sun	medium	small	8
Natural creatures, mushrooms	~78% under 1 sun	low	small	9
Plasmonic biofoams based on bacterial nanocellulose or reconstituted silkworm silk.	76.3% under 5.1 sun	medium	medium	10
a carbon foam (10-mm thick) supporting an exfoliated graphite layer (5-mm thick)	64% under 1 sun, 85% under 10 sun	medium	medium	11
Vertically aligned graphene sheets membrane	86.5% under 1 sun, 94.2% under 4 sun	medium	small	12
Al_2O_3 coated outside of Au nanoparticles	65% under 4 sun	high	small	13
CNT/GO layer/graphene oxide/nanofibrillated cellulose (GO/NFC)/ GO/NFC wall	85.6% under 1 sun	high	medium	14
Gold plasmonic nanostructures	87% under 2.3 sun	high	small	15
carbon nanotube (CNT) modified filter paper	75% under 1 sun	high	medium	16
RGO/ polystyrene	83% under 1 sun	high	medium	17

Reference:

[1] L. Zhou, Y. Tan, J. Wang, W. Xu, Y. Yuan, W. Cai, S. Zhu, J. Zhu, *Nat. Photon.* **2016**, *10*, 393.

[2] Y. Liu, S. Yu, R. Feng, A. Bernard, Y. Liu, Y. Zhang, H. Duan, W. Shang, P. Tao, C. Song, T. Deng, *Adv. Mater.* **2015**, *27*, 2768.

[3] Q. Jiang, L. Tian, K. K. Liu, S. Tadepalli, R. Raliya, P. Biswas, R. R. Naik, S. Singamaneni, *Adv. Mater.* **2016**, *28*, 9400.

[4] Y. Liu, J. Chen, D. Guo, M. Cao, L. Jiang, *ACS Appl. Mater. Interfaces*. **2015**, *7*, 13645.

[5] J. Wang, Y. Li, L. Deng, N. Wei, Y. Weng, S. Dong, D. Qi, J. Qiu, X. Chen,T. Wu, *Adv. Mater.* **2017**, *29*, 1603730.
[6] X. Hu, W. Xu, L. Zhou, Y. Tan, Y. Wang, S. Zhu, J. Zhu, *Adv. Mater.* **2017**, *29*, 1604031.
[7] X. Li, W. Xu, M. Tang, L. Zhou, B. Zhu, S. Zhu, J. Zhu, *PNAS*, **2016**, 113, 13953.
[8] Y. Ito, Y. Tanabe, J. Han, T. Fujita, K. Tanigaki, M. Chen, *Adv. Mater.* **2015**, *27*, 4302.
[9] N. Xu, Xiaozhen Hu, W. Xu, X. Li, L. Zhou, S. Zhu, J. Zhu, *Adv. Mater.* **2017**, *29*, 1606762.
[10] L. Tian, J. Luan, K.K. Liu, Q. Jiang, S. Tadepalli, M. K. Gupta, R. R. Naik, S. Singamaneni, Nano Lett. **2016**, *16*, 609.
[11] H. Ghasemi, G. Ni, A. M. Marconnet, J. Loomis, S. Yerci, N. Miljkovic, G. Chen, *Nat. Commun.* **2014**, *5*, 4449.
[12] P. Zhang, J. Li, L. Lv, Y. Zhao, L. Qu, *ACS Nano*. **2017**, *11*, 5087.
[13] L. Zhou, S. Zhuang, C. He, Y. Tan, Z. Wang, J. Zhu, *Nano Energy*. **2017**, *32*, 195.
[14] Y. Li, T. Gao, Z.Yang, C. Chen, W. Luo, J. Song, E. Hitz, C. Jia, Y. Zhou, B. Liu, B. Yang, L. Hu, *Adv. Mater.* **2017**, *29*, 1700981.
[15] C. Liu, J. Huang, C. E. Hsiung, Y. Tian, J. Wang, Y. Han, A. Fratalocchi, *Adv. Sustainable Syst.* **2017**, *1*, 1600013.
[16] P. Yang, K.Liu, Q. Chen, J. Li, J. Duan, G. Xue, Z. Xu, W. Xie, J. Zhou, *Energy Environ. Sci.*, **2017**, DOI: 10.1039/C7EE01804E.
[17] L. Shi, Y. Wang, L. Zhang, P. Wang, *J. Mater. Chem. A*, **2017**, *5*, 16212.